applied optics

Phase-ratio imaging as applied to desert sands for tracking human presence

Alex J. Yuffa,[1] Vadym Kaydash,[2] Viktor Korokhin,[2] Yuriy Shkuratov,[2] Evgenij Zubko,[3] and Gorden Videen[1,*]

[1]Army Research Laboratory AMSRL-CI-EM, 2800 Powder Mill Road, Adelphi, Maryland 20783, USA
[2]Institute of Astronomy, Kharkiv V. N. Karazin National University, 35 Sumskaya St., Kharkiv 61022, Ukraine
[3]School of Natural Sciences, Far Eastern Federal University, 8 Sukhanova St., Vladivostok 690950, Russia
*Corresponding author: Gorden.W.Videen.civ@mail.mil

Received 22 July 2016; revised 11 October 2016; accepted 25 November 2016; posted 29 November 2016 (Doc. ID 272187); published 9 January 2017

The phase function is a measure of the light-scattered intensity, or radiance, as a function of scattering angle θ. A phase ratio is the ratio of two values of the phase function measured at different scattering angles and relates to the slope of the phase function. By taking the ratio of two images acquired at different illumination or observation conditions, a phase-ratio image can be constructed. Such images accentuate differences in the phase curves, rather than their intensities, and are more sensitive to microtopography than to material properties. We produce phase-ratio images from intensity images acquired at different observation times and locations in the desert environment of White Sands National Monument. Because of the lack of surface features, coregistration of the images is challenging, especially for images acquired from different observation locations. However, we do demonstrate that phase-ratio images can be used to identify disturbed sands. We also produce polarimetric and color-ratio images. These latter images do not suggest the possibility of identifying topographical differences due to human presence.

OCIS codes: (100.0100) Image processing; (280.0280) Remote sensing and sensors; (290.5880) Scattering, rough surfaces; (290.5855) Scattering, polarization.

https://doi.org/10.1364/AO.56.00B184

1. INTRODUCTION

The properties of light scattered from a surface depend on the observing conditions, especially the location of the light source and observer. For many applications, it is common to express the light scattering as a function of the phase angle α, which is the angle subtended between the vector that connects the source to the surface and the vector that connects the surface to the observer [Fig. 1(a)]. Note that the phase angle α is measured from the exact backscattering direction and is related to the scattering angle θ by $\alpha = 180° - \theta$. The resulting phase curve [Fig. 1(b)] is a measure of the scattering property as a function of phase angle α. Most typically, the phase curve is the intensity of light scattered from the surface, but it can also be a measure of other properties, such as a polarization state as a function of phase angle α.

The light scattered from surfaces is a property of the material composition and the surface topography (e.g., [1]). A flatter, smoother surface usually has an intensity phase function that is steep [curve 1 in Fig. 1(b)]; whereas a rougher, more structured surface usually has a flatter, more isotropic phase function [curve 2 in Fig. 1(b)]. A phase ratio is constructed simply by taking the ratio of the surface albedos measured at two different phase angles: $f(\alpha_1{:}\alpha_2) = I(\alpha_1)/I(\alpha_2)$. The phase ratio is a characterization of the slope of the phase curve, which has a weak dependence on the absolute surface albedo, which is largely dependent on the material composition. Hence, the phase curve is primarily dependent on the surface topography, although we find that there still exists some dependence on the material properties. For instance, for the Moon, the albedo and phase ratio are still correlated [2]. Phase-ratio imaging has been used almost exclusively in planetary science.

Phase-ratio imaging is performed by creating a phase ratio for every point of an image. To do this, two images are needed that have been acquired at two different phase angles: α_1 and α_2 [3]. The incident and observation angles, i and e, respectively, are measured from a surface normal **n**, as shown in Fig. 1. For a nonplanar surface, the assignment of a surface normal is somewhat arbitrary. The different phase angles can be achieved by changing the incident angle [i in Figure 1(a)], the observation angle [e in Fig. 1(a)] or both angles simultaneously. There are advantages and disadvantages to all these methods. If the incident angle is changed, then each pixel of

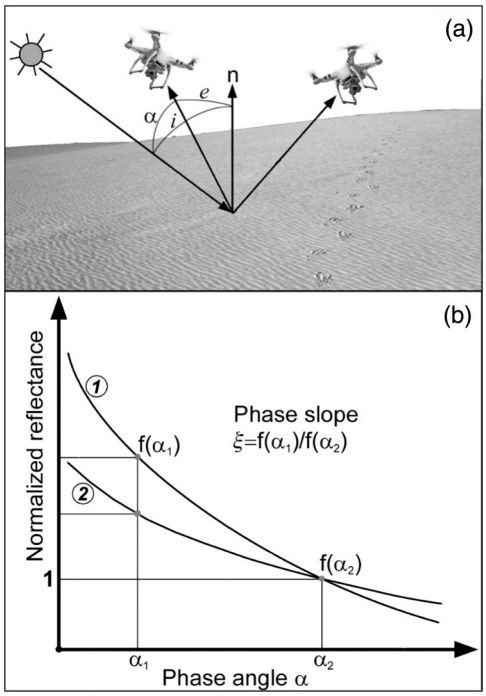

Fig. 1. (a) Illumination/observation geometry for acquiring phase-ratio images; (b) Light-scattering phase function depends on material and surface topography.

both images maps to the same surface location, and all that is required to create the phase-ratio image is to take the ratio of the intensity measured at each location. If the observation angle is changed, then the pixels are not coaligned and a coregistration process is needed to map the pixels of one image onto those of the other image. To do this, a rubber-sheet geometric transformation is used [4]; this is a very important step in providing high-quality results. While the accuracy of the coregistration process can be as high as 1/10 of a pixel, achieving such accuracy depends on identifying and collocating identifying features in both images. In relatively uniform images, the collocation and subsequent coregistration can be challenging or even impossible. One advantage of using two images acquired at different observation angles is that a transformation can be made onto either or both perspectives, so that a phase-ratio image can be obtained from the perspective of either observation position. With this information, a three-dimensional anaglyph image can be constructed [3], providing additional information about larger-scale surface topography.

One way to study the structure of a light-scattering surface is by comparing its imaging parameters with those of a model. The model may be empirical [2,5–7] or theoretical [2]. The field of phase-ratio imagery blossomed when the rich archive of images acquired from orbiting spacecraft, such as the Lunar Reconnaissance Orbiter (LRO), was exploited. They have been used to characterize and map craters Giordano Bruno [3], Kepler and Cauchy [4], Copernicus [6], Denning [8], and Reiner *G*, Godin, and Grimaldi [9]. The technique has been used to identify photometric anomalies in Oceanus Procellarum that might be due to swarm impacts [10]. On Mercury, messenger images have been used to examine melt flows, pyroclastic deposits, and impact craters [11].

Most relevant to our study has been the use of phase-ratio imaging to examine anthropogenic influences on the lunar surface. Several studies have used the technique to examine the landing and impact sites of spacecraft. The dust cloud kicked up and resettled on the surface by the landing jets of the Luna and Apollo modules has a distinct signature characterized by a shallower phase curve than that of the surrounding regions [8,11–16]. Spacecraft impact sites create craters and rays from excavated materials. Phase-ratio imaging suggests that these features have higher surface roughness than the surrounding regions [8].

The other anthropogenic features made more apparent through phase-ratio imaging are the tracks left by the Apollo astronauts themselves: either their footpaths or the tracks left by the lunar vehicles [14,15]. Unlike the landing jets or spacecraft impacts, these anthropogenic interactions compact the lunar regolith. This compaction results in a stronger specular reflection, which can be seen in the Apollo 14 images produced by Kaydash *et al.* [13]. The compacted regolith has a steeper phase curve than that of the surrounding region, and these tracks can be enhanced through phase-ratio imaging.

The question we consider is whether such anthropogenic effects can be enhanced on Earth using phase-ratio imaging. While it seems that the same considerations would apply, the terrestrial and lunar regoliths are very different. Unlike terrestrial soils and sands, lunar regolith has a different structure and is formed under different forces. Due to adhesion forces, lunar regolith particles can attach to each other at single points, forming what has been described as a fairy castle structure [1,17], having porosities higher than 50% and extending tens of millimeters beneath the surface. The compaction effect due to the boots and tires of the Apollo mission on such material is significantly different from that of terrestrial dry sands. We would expect the change of porosity to be one of the greatest factors in detecting tracks from the lunar regolith, and this factor would not be present on Earth. One commonality of tracks on the Earth and Moon are shadows. As the phase angles increase from the exact-backscattering direction, shadows rapidly grow, causing a steeper phase curve, but this effect is most significant at small phase angles. The purpose of our study is to determine if phase-ratio imaging could be used to detect human presence in a terrestrial desert environment. The applications of such a technique include tracking and improvised explosive device (IED) detection. We expect, however, that the technique can find many applications to determine the extent of processes that can change the morphology of a system. Such applications include, for instance, differentiating and characterizing different lava features, examining weathering and streamer features on dunes, or identifying different types of land use. Such features can be difficult to map using traditional albedo-based remote-sensing techniques that are more sensitive to material differences than morphological differences.

2. OBSERVATIONS

We selected the terrain of White Sands National Monument (WSNM) and obtained images on 2 June 2016. The

WSNM contains dunes of windblown gypsum sands. The dunes are tens of meters high, facilitating image acquisition of one dune from a neighboring dune. We searched for a location toward the back of the park, where the dunes are known to be larger, and selected two relatively pristine dune surfaces that did not have obvious anthropogenic influence. One dune surface was in the sunward direction, resulting in a relatively large phase angle. The other dune surface was selected away from the sun and had a smaller phase angle. Because of the duneous terrain, altitude was not constant between sites, so the phase angle could only be determined approximately. Yardsticks were used as reference markers on both scenes, and the GPS positions of these sticks, camera locations, and times were recorded. Tracks were made across the scenes when the markers were placed in the ground. For each scene, images were captured from two different locations. The image acquisition process began at approximately 3:30 p.m. local time. Two dunes were imaged, each at two different camera locations. Each set of images was captured in two different camera settings and three different linear polarization states, making a total of 24 images. It took approximately 30 min to acquire one complete set of images. More detail on the types of images we acquired is given in Section 3 below. The process was repeated at 4:55 p.m. local time to allow the sun to traverse and change the incident angle. This allowed for the possibility of creating phase-ratio images through changes of both incident and observation angles. Table 1 shows the site information data for the two scenes.

For image acquisition, we used a Canon T1i DSLR equipped with an 18–55 mm zoom lens. We took all pictures with the focal length setting of 55 mm. Due to the brightness of the white sands, we could not read the camera panels, so we took pictures in the automatic and program settings using both raw and JPEG formats. The image exposures were normalized during processing using the settings recorded in the image data files.

Since camera detectors tend to favor one polarization state, we equipped the lens with a circular polarizer composed of a linear polarizer facing the scene and a quarter-wave plate facing the detector. This effectively created a linear analyzer. A series of three images was captured, with this analyzer rotated 60° between images. This allowed the possibility of constructing the Stokes parameters or any linear polarization property of the scattered light through the Fesenkov formulae [18]. In addition, the CMOS sensor in the camera allows for the possibility of decomposing the light into red, green, and blue components, allowing the possibility of considering color ratios.

Pixel-to-pixel variations of the sensor response were corrected through calibration. Focused and defocused images of skylight captured at different exposure times and apertures were used to map the pixel variations. A large number of images were captured to consider different image-processing options and contingencies. However, if our goal was only to produce phase-ratio images, we found and demonstrated that an adequate phase-ratio image could be obtained from any two of the images taken at different observation positions.

Table 1. Coordinates of Camera Positions and Markers

Scene		GPS Reading	GPS Reading
1	Camera 1	N32.82652°	W106.27750°
1	Camera 2	N32.82652°	W106.27753°
1	Marker 1	N32.82651°	W106.27828°
1	Marker 2	N32.82677°	W106.27841°
1	Marker 3	N32.82672°	W106.27813°
1	Marker 4	N32.82653°	W106.27807°
2	Camera 3	N32.82652°	W106.27753°
2	Camera 4	N32.82655°	W106.27739°
2	Marker 5	N32.82715°	W106.27749°
2	Marker 6	N32.82768°	W106.27738°
2	Marker 7	N32.82715°	W106.27729°

A. Phase Angles

To produce phase-ratio images, it is not necessary to know the actual phase angles, only to know that they have changed. However, since we are performing an assessment of the technique, it is valuable to know the approximate phase angles used. Because the distance from the dune to the camera is relatively short, phase angle varies significantly over the field. We calculate the phase angles at the marker positions observed from the different camera positions for reference.

We use the NOAA Solar Calculator [19] to retrieve the solar azimuth, relative to the North Pole, calculated clockwise, and solar elevation for the given date and time. Thus, for 2 June 2016 (3:30 p.m.) we retrieve solar azimuth = 270.66° and solar elevation = 43.48°. For 2 June 2016 (4:55 p.m.) we retrieve solar azimuth = 281.02° and solar elevation = 25.76°. These values are used for all seven markers (sticks) in the frames obtained for the two survey areas. Figure 2 shows the GPS positions of the markers in the frame and camera positions for survey areas 1 and 2. The arrow indicates north.

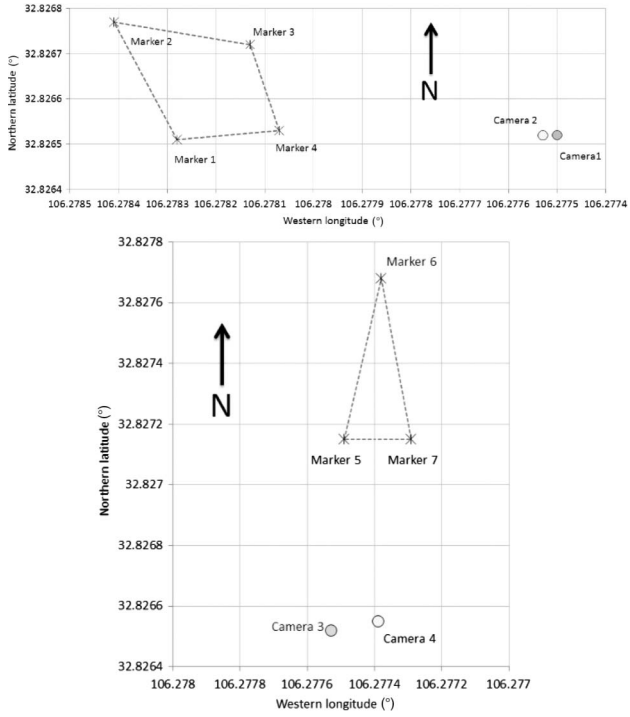

Fig. 2. Maps showing the stick positions in the field of Scene 1 (top) and Scene 2 (bottom), and the approximate camera positions.

Note the first area was imaged from the eastern direction, while the second area was imaged from the southern direction.

We did not survey the slope of the dune, nor of the camera positions, so relative altitudes are unknown. Based on the images and size of the markers, the dunes are approximately 10 m in height. The lack of altitude information is a source of error because the phase angle also depends on differences in altitude between the object and image. The incident angle can be obtained from the solar elevation: $i = 90$ solar elevation, and the angular distance between the markers in the frame and the camera on the spherical Earth can be calculated using

$$\theta = \text{acos}[\sin(b_{\text{stick}}) \cdot \sin(b_{\text{camera}}) + \cos(b_{\text{stick}}) \cdot \cos(b_{\text{camera}}) \cdot \cos(l_{\text{stick}} - l_{\text{camera}})], \quad (1)$$

where b is the latitude and l is the longitude of the stick (marker) or camera. The linear distance can be obtained by multiplying this value by 111.11 km/° to convert the angular extent to distance. If we assume the camera is 2 m above the ground, we can calculate the emission angle

$$e = \sin(b_{\text{stick}}) \cdot \sin(b_{\text{camera}}) + \cos(b_{\text{stick}}) \cdot \cos(b_{\text{camera}}) \cdot \cos(l_{\text{stick}} - l_{\text{camera}}). \quad (2)$$

From the spherical triangle defined by the North Pole, stick, and camera, we can calculate the angle between two directions, defined, for instance, by the vector connecting the camera and a stick marker and the camera and the North Pole by

$$\beta = \cos^{-1}\left\{\frac{\cos(\theta_{\text{NP-stick}}) - \cos(\theta_{\text{Camera-stick}}) \cdot \cos(\theta_{\text{NP-camera}})}{\sin(\theta_{\text{Camera-stick}}) \cdot \sin(\theta_{\text{NP-camera}})\cdot}\right\}, \quad (3)$$

where the subscripts refer to the angular distances between the corresponding sticks, camera position, and North Pole (NP). The azimuthal angle between planes of scattering and incidence is calculated as $\phi =$ solar azimuth β, taking into account the clockwise calculated solar azimuth. Finally, the phase angle α can be calculated using

$$\cos\alpha = \cos i \cos e + \sin i \sin e \cos\phi. \quad (4)$$

In Table 2, we list the phase angles at the marker positions calculated from the different camera positions and times. We emphasize that these phase angles do not include the effect of altitude, which can be significant. Note that the phase angle varies by a few degrees for the different markers shown in the images in each scene. This means that the phase angle is not constant for a given picture, but varies across the image.

The finite extent of the sun reduces only slightly the sensitivity of phase-ratio imaging, as our measurement is an integration of a portion of the phase curve. For very small differences in incident or observation angle $< 1°$, this can reduce the fidelity of the processed images, but usually this is not an issue.

Table 2. Phase Angles Measured from Each Source and Marker at the Two Different Observations Times

		Phase Angles			
		Camera Position 1, 3		Camera Position 2, 4	
Scene	Marker	3:30 p.m.	4:55 p.m.	3:30 p.m.	4:55 p.m.
1	1	135°	151°	135°	151°
1	2	132°	141°	132°	141°
1	3	131°	139°	130°	138°
1	4	134°	150°	134°	150°
2	5	90°	97°	98°	107°
2	6	88°	94°	92°	99°
2	7	78°	83°	86°	92°

3. IMAGES

Figure 3 shows processed images taken of Scene 1. Figure 3(a) shows the total intensity that is constructed from the three different linearly polarized images of the scene at approximately 3:30 p.m. This image was taken at a large phase angle ($\alpha \sim 140°$), and the sun was located in the upper left of the image. The dune face has a windswept, corrugated wave structure, whose waves appear to travel predominantly in the horizontal direction of the image across the dune. The four markers are plainly visible, with tracks of footprints going vertically between them and one set diagonally across the dune from lower right to upper left. The dune itself contains a ridge. The lower portion is steeper and receives less afternoon illumination. Across this darker region are a number of tracks created by darkling beetles. Although clouds appear in the background of this image, cloud cover existed only over the mountains near the horizon. The sky above the Tularosa Basin was clear and the illuminating sunlight was unrestricted during the entire observation campaign. During the campaign, the observers encountered a number of whiptail lizards and darkling beetles that could have disturbed the field during the campaign. One western diamondback rattlesnake, that was well over 2 m long, was observed crossing the road upon exiting the monument, at which point the corresponding author was informed that if any additional data were needed, he would be taking that data without assistance.

Figure 4 shows processed images taken of Scene 2. In this figure, the camera faces a northerly direction. The phase angle α is smaller than that of the images of Fig. 3 (see Table 2) and the Sun is behind and to the left of the photographer. The dune of Scene 2 has a more constant slope than that of Scene 1, with no steep sections. It also receives sunlight more directly, at a very low incident angle, so the shadows are much weaker than in Scene 1. Note that where the tracks are quite apparent through shadowing in Fig. 3(a), they are not obvious in Fig. 4(a).

The remaining panels of images show phase-ratio [Figs. 3(b) and 4(b)], color ratio [Figs. 3(c) and 4(c)] and cross-polarization [Figs. 3(d) and 4(d)] images. A large number of other images were processed, including using differencing techniques between images, and ratios of images of different colors of different polarization states. We do not display them because we found they did not provide additional information that was achieved here. In addition, these additional image-processing techniques are not common.

A. Phase-ratio Images Using Different Incident Angles

Phase-ratio images created from images with changing incident angle are shown in Figs. 3(b) and 4(b). These images are created

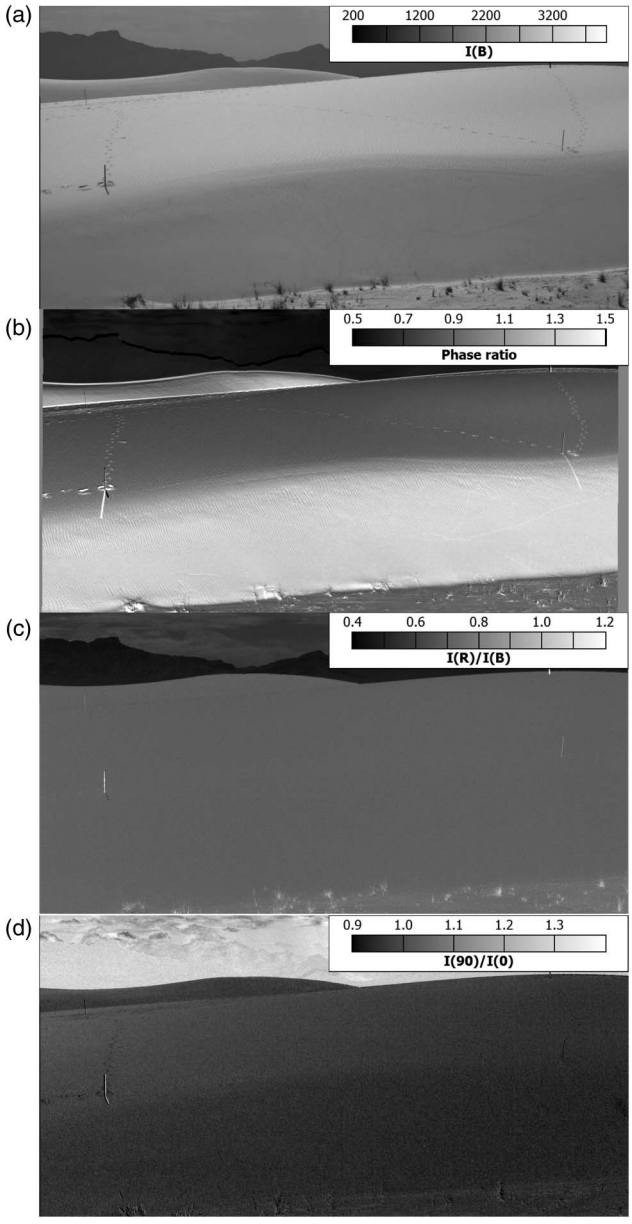

Fig. 3. Processed images from Scene 1. (a) Full-intensity image as recorded in green light; (b) phase-ratio image created from images captured with different incident angles; (c) color-ratio images; and (d) cross-polarization ratios in blue light. Details may be significantly more apparent in printed versions of the images.

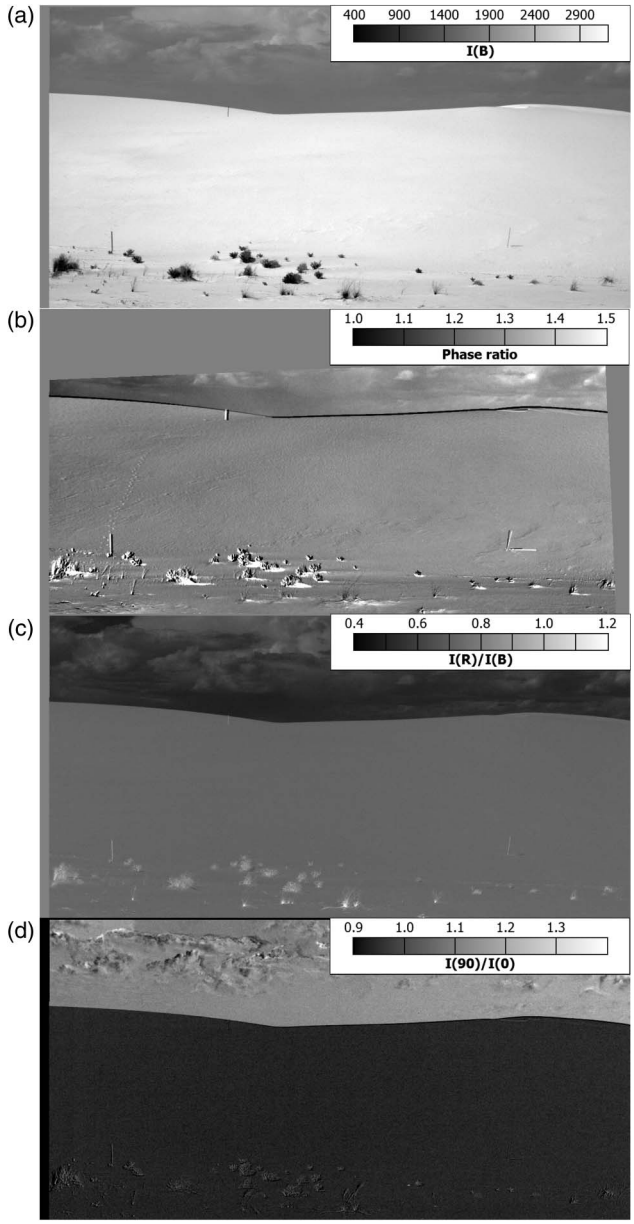

Fig. 4. Processed images from Scene 2. (a) Full-intensity image as recorded in blue light; (b) phase-ratio image created from images captured with different incident angles; (c) color-ratio images; and (d) cross-polarization ratios in blue light.

by taking images from the same location at a different time. In this paper, the image-acquisition process was repeated after approximately 85 min, resulting in a phase angle change of approximately 10–15°, depending on the field position. Because the camera position was not constant, but had been moved to different locations to make other images, the frames are not identical. Because of these changes, coregistration of the images is not precise. The border regions between the dune and mountain and the mountain and sky [Fig. 3(b)] and between the dune and sky [Fig. 4(b)] demonstrate imperfections in the coregistration process.

Figure 3(b) shows the phase ratio of the dune having a larger phase angle. The tracks in the upper portion of the dune appear slightly enhanced from the intensity image of Fig. 3(a). In the lower portion, the dune striations are much more apparent in the phase-ratio image. In addition, the network of tracks from the darkling beetles is also visible. These features can be made visible, although not as prominent, in the intensity image by underexposing the image, as in Fig. 5(a). In Fig. 5(a), the contrast is increased by decreasing the exposure of the image. Albedo normalization is inherent in producing phase-ratio images, so additional steps to increase the contrast are not essential.

Figure 4 was taken at a much smaller phase angle (Table 2). As such, the shadows from the footprints and structures of the dune are very weak, and such features are barely visible in the intensity image [Fig. 4(a)]. The phase-ratio image of Fig. 4(b) has enhanced these features. Footprints are visible on the left portion of the frame between the two stakes, and structure in the dune surface is visible, including indentations and variations in surface roughness.

B. Color-ratio Images

While color-ratio images are not the main topic of this article, they are commonly used in remote-sensing applications. We show them here for comparison purposes. Color-ratio images can be produced from a single image by considering the signals recorded by the individual color components recorded by the camera. In this case, we take the ratio of the signal captured by the red pixel divided by that of the accompanying blue pixel. In theory, we can imagine that color-ratio images can be useful for detecting shadowed regions. While directly illuminated regions of the sand are quite white, regions shadowed from direct sunlight would receive secondary illumination from other sources (e.g., from surrounding sunlit surfaces). We also would anticipate a significant component of this illumination to be blue skylight, providing shadowed regions with a bluish hue. We might expect such regions to be dimmer in color-ratio images.

Sample color-ratio images are shown in Figs. 3(c) and 4(c). As can be seen in these images, the color ratios of the dunes appear quite uniform. The footprints that are obvious in the albedo and phase-ratio images are not apparent. In addition, we can see no differentiation in the images where there are obvious differences in the morphology. For instance, the base and ridge of the dune (in Fig. 3) have significantly different morphologies, yet the color-ratio image appears nearly featureless. It is not even easy to distinguish the dune in the foreground of Fig. 3(c) from that in the background. In addition to these images, we also considered color-ratio images produced using polarized light. In none of the color-ratio images that we produced were changes in surface morphology obvious.

C. Polarization

All of our images were obtained with an analyzer consisting of a linear polarizer and quarter-wave plate, which collected the light of a specific linear polarization state. We rotated the analyzer 60° and 120° to capture a series of three images from which all the linear-polarization states could be constructed. We constructed ratio images of color and phase using different polarization states, and also Stokes-parameter images Q and U, in addition to cross-polarization ratios. We did not see an advantage in considering polarization in the production of ratio images of color and phase. These images looked very similar to those that have been reproduced in Fig. 3(b), 3(c), 4(b), and 4(c).

To produce cross-polarization images, we considered the image made from light polarized at 90° (horizontal) and divided it by the image made from light polarized at 0° (vertical). The theory behind the use of this parameter for detecting tracks is as follows. Light scattered from a smooth surface tends to be positively polarized. Surface irregularities introduce sloped components that are different from the natural dune slope. These irregularities will scatter light of a different polarization state from that of the natural slope. We would expect these changes would be reflected in the cross-polarization images and the Stokes-parameter images. Figure 3(d) shows cross-polarization images captured using the blue-sensitive pixels (red-pixel images are similar). We can see the footprints going down the slope on the left portion of the images, but other surface features are not obvious. In Fig. 4(d), it is difficult to discern any surface morphology. We suspect this is because the effect of slope may increase with phase angle α. The Stokes-parameter images looked very similar to these images and are not shown here.

D. Phase-ratio Images Using Different Observation Positions

Because of its utility, one goal of this work was the production of phase-ratio images from different observation positions. Such images have been made routinely using the LRO satellite orbiting the Moon. Unfortunately, the procedure of making phase-ratio images in the white sands of New Mexico was challenging. In order to take into account the local topography, a rubber-sheet algorithm is used to coregister the pixels, placing them onto a common coordinate system [4]. In order to operate the algorithm, it is necessary to identify common features in both images. Such features can be rocks, outcrops, plants, etc. Unfortunately, the dune surfaces selected were composed of relatively featureless gypsum sand. We were able to produce one set of coregistered images using the outline of the ridge of the dune in Scene 1 [Fig. 5(a)]. Using this outline, we were able to produce the phase-ratio image of Fig. 5(b). Due to the slope on this part of the dune, we were unable to traverse this section;

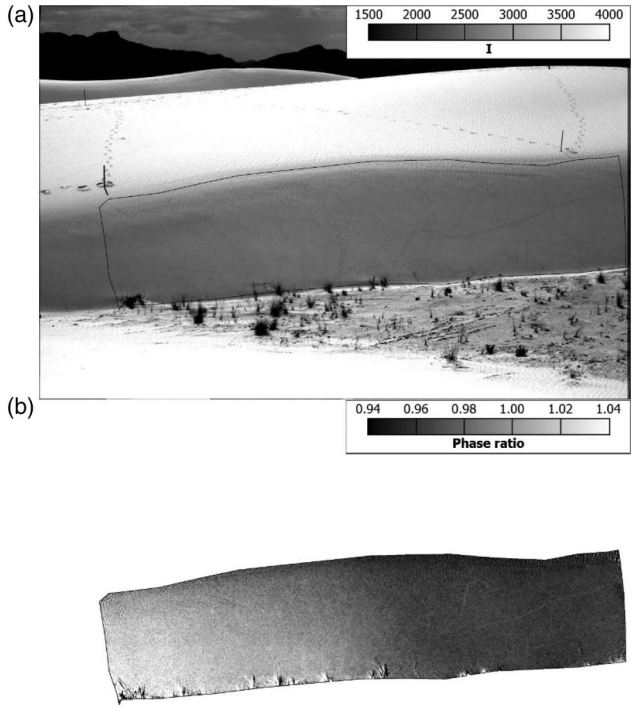

Fig. 5. Total intensity image (a) showing region in which it was possible to produce observation-angle-dependent phase-ratio image shown in (b).

however, there did exist a network of tracks left by darkling beetles. These tracks can be seen in both the albedo and phase-ratio images shown in Fig. 5.

4. CONCLUSION

We have taken a series of images of desert dunes at different phase angles and considered whether different imaging techniques could be used to detect human tracks. The least useful for our purposes was color-ratio imaging. While this technique could be useful if the composition of the tracks were different from the surrounding terrain, this was not the case for the gypsum sands we analyzed. While polarization either expressed as a ratio or examining the pure Stokes vectors could discern tracks, their utility did depend on the phase angles. Incorporating polarization did not appear to provide significant enhancement. For instance, a ratio of polarized red light to polarized blue light did not provide any enhancement to the red-to-blue color-ratio image.

The phase-ratio image captured with changing incident angle was able to discern tracks on both the dunes we imaged. It was able to detect tracks made at relatively small phase angles where the tracks were not obvious in the albedo images. Unfortunately, due to the featureless nature of the WSNM, we were not able to use the rubber-sheet algorithm effectively in order to produce a series of phase-ratio images using different observation angles. The image that we did produce did not contain any regions containing human footprints; however, the technique did image the tracks of darkling beetles that were present.

In summary, we have demonstrated that phase-ratio images can be used to detect human tracks in terrestrial sands. While we did demonstrate their utility at two different phase-angle regions, we expect the sensitivity to depend on the portion of the phase curve examined. Phase function is a measure of the slope of the phase curve, which can change dramatically with phase angle, even changing sign. At extremely small phase angles, we expect different sensitivity than at intermediate or grazing angles. Although we considered two different regions of the phase curve, they both could be considered to be at intermediate angles. To produce high-quality phase-ratio images, it is necessary to examine regions having more features so that the rubber-sheet algorithm can be used effectively. This will be a topic of future research.

Funding. Army Research Office (ARO) (W911NF-16-2-0111).

REFERENCES

1. B. Hapke, *Theory of Reflectance and Emittance Spectroscopy* (Cambridge University, 1993), p. 450.
2. Y. Shkuratov, V. Kaydash, V. Korokhin, Y. Velokodsky, N. Opanasenko, and G. Videen, "Optical measurements of the Moon as a tool to study its surface," Planet. Space Sci. **59**, 1326–1371 (2011).
3. Y. Shkuratov, V. Kaydash, and G. Videen, "The lunar crater Giordano Bruno as seen with optical roughness imagery," Icarus **218**, 525–533 (2012).
4. V. Kaydash, Y. Shkuratov, and G. Videen, "Phase-ratio imagery as a planetary remote-sensing tool," J. Quant. Spectrosc. Radiat. Transfer **113**, 2601–2607 (2012).
5. R. L. Wildey, "The moon in heiligenschein," Science **200**, 1265–1267 (1978).
6. Y. Shkuratov, V. Kaydash, L. Rohacheva, V. Korokhin, M. Ivanov, Y. Velikodsky, and G. Videen, "Comparison of lunar red spots including the crater Copernicus," Icarus **272**, 125–139 (2016).
7. V. Korokhin, Y. Shkuratov, V. Kaydash, and G. Videen, "Characterization of a photometric anomaly in lunar Mare Nubium," Planet. Space Sci. **122**, 70–87 (2016).
8. V. Kaydash, Y. Shkuratov, and G. Videen, "Dark halos and rays of young lunar craters: a new insight into interpretation," Icarus **231**, 22–33 (2014).
9. Y. I. Velikodsky, V. V. Korokhin, Y. G. Shkuratov, V. G. Kaydash, and G. Videen, "Opposition effect of the Moon from LROC WAC data," Icarus **275**, 1-15 (2016).
10. V. G. Kaydash, S. Y. Gerasimenko, Y. G. Shkuratov, N. V. Opanasenko, Y. I. Velikodskii, and V. V. Korokhin, "Photometric function variations observed on the near side of the Moon: mapping," Solar Syst. Res. **43**, 89–99 (2009).
11. D. T. Blewett, C. L. Levy, N. L. Chabot, B. W. Denevi, C. M. Ernst, and S. L. Murchie, "Phase-ratio images of the surface of Mercury: evidence for differences in sub-resolution texture," Icarus **242**, 142–148 (2014).
12. Y. Shkuratov, V. Kaydash, X. Sysolyatina, A. Razim, and G. Videen, "Lunar surface traces of engine jets of Soviet sample return probes: the enigma of the Luna-23 and Luna-24 landing sites," Planet. Space Sci. **75**, 28–36 (2013).
13. V. Kaydash, Y. Shkuratov, and G. Videen, "Landing of the probes Luna 23 and Luna 24 remains an enigma," Planet. Space Sci. **89**, 172–182 (2013).
14. V. Kaydash, Y. Shkuratov, V. Korokhin, and G. Videen, "Photometric anomalies in the Apollo landing sites as seen from the Lunar Reconnaissance Orbiter," Icarus **211**, 89–96 (2011).
15. R. N. Clegg, B. L. Jolliff, M. S. Robinson, B. W. Hapke, and J. B. Plescia, "Effects of rocket exhaust on lunar soil reflectance properties," Icarus **227**, 176–194 (2014).
16. R. N. Clegg-Watkins, B. L. Jolliff, A. Boyd, M. S. Robinson, R. Wagner, J. D. Stopar, J. B. Plescia, and E. J. Speyerer, "Photometric characterization of the Chang'e-3 landing site using LROC NAC images," Icarus **273**, 84–95 (2016).
17. B. Hapke and H. van Horn, "Photometric studies of complex surfaces with applications to the moon," J. Geophys. Res. **68**, 4545–4570 (1963).
18. V. G. Fesenkov, Astron. Zh. **12**, 309 (1935).
19. "NOAA Solar Calculator," http://www.esrl.noaa.gov/gmd/grad/solcalc/.